

# Serial two-photon tomography for automated *ex vivo* mouse brain imaging

Timothy Ragan<sup>1,4</sup>, Lolahon R Kadiri<sup>2,4</sup>,  
Kannan Umadevi Venkataraju<sup>2</sup>, Karsten Bahlmann<sup>1</sup>,  
Jason Sutin<sup>1</sup>, Julian Taranda<sup>2</sup>, Ignacio Arganda-Carreras<sup>3</sup>,  
Yongsoo Kim<sup>2</sup>, H Sebastian Seung<sup>3</sup> & Pavel Osten<sup>2</sup>

**Here we describe an automated method, named serial two-photon (STP) tomography, that achieves high-throughput fluorescence imaging of mouse brains by integrating two-photon microscopy and tissue sectioning. STP tomography generates high-resolution datasets that are free of distortions and can be readily warped in three dimensions, for example, for comparing multiple anatomical tracings. This method opens the door to routine systematic studies of neuroanatomy in mouse models of human brain disorders.**

Since the pioneering work of Ramón y Cajal, advances in light microscopy have been central to many discoveries in neuroanatomy. The recent focus on systematic generation of whole-brain datasets, for example, the Allen Mouse Brain Atlas for gene expression<sup>1</sup> and the ongoing Mouse Brain Architecture Project for mesoscopic connectivity<sup>2</sup>, has created a pressing need for the development of new instrumentation for high-throughput whole-brain imaging. Here we describe a microscopy method, STP tomography, that enables automated high-throughput imaging of fluorescently labeled mouse brains. This method uses whole-mount two-photon microscopy<sup>3,4</sup> and thus generates datasets of well-aligned, high-resolution serial optical sections. We tested the versatility of STP tomography by imaging four mouse brains with cell type-specific fluorescent protein expression and by systematically mapping input and output connections of mouse somatosensory cortex. These experiments show that STP tomography is a robust imaging method that can transform the emerging field of systematic whole-brain anatomy, until now limited to dedicated atlas-generation initiatives<sup>1,2</sup>, into a routine methodology applicable, for example, to the study of mouse models of human brain disorders in standard laboratory settings.

STP tomography works as follows (Fig. 1 and Supplementary Video 1). First, a fixed agar-embedded mouse brain is placed in a water bath on integrated *x-y-z* stages under the objective of a two-photon microscope, and imaging parameters are entered in

the operating software (Online Methods). Once these are set, the instrument works fully automatically: (i) the *x-y-z* stages move the brain under the objective so that an optical section (or an optical *z* stack) is imaged as a mosaic of fields of view (FOVs), (ii) a built-in vibrating blade microtome mechanically cuts off a tissue section from the top and (iii) the steps of overlapping optical and mechanical sectioning are repeated until the dataset is collected. The instrument is based on a previous prototype<sup>4</sup>, which we redesigned for imaging of fluorescently labeled mouse brains, including the integration of a custom-built vibrating blade microtome instead of a milling machine and the use of high-speed galvanometric scanners instead of a rotating polygonal scanner (Online Methods). Sectioning by vibrating blade microtome allows the use of brains prepared by formaldehyde fixation and agar embedding, which have minimal detrimental effects on fluorescence and brain morphology. High-speed galvanometric scanning enables fast imaging at different sampling resolutions.

In the first experiments, we used *Thy1-GFP* (line M) mice, which express GFP mainly in hippocampal and cortical pyramidal neurons, to determine the optimal conditions for imaging mouse brains at different sampling resolutions. We imaged the brain from a *Thy1-GFP* mouse as a dataset of 260 coronal sections, evenly spaced by 50  $\mu\text{m}$ , with 10 $\times$  and 20 $\times$  objectives at *x-y* imaging resolution 2.0  $\mu\text{m}$ , 1.0  $\mu\text{m}$  and 0.5  $\mu\text{m}$  (Fig. 1, Supplementary Figs. 1–3 and Supplementary Video 2). The 10 $\times$  objective (0.6 numerical aperture (NA)) allowed fast imaging at a resolution sufficient to visualize the distribution and morphology of GFP-labeled neurons, including their dendrites and axons (Supplementary Figs. 2–3). The data collection times for a 10 $\times$ -objective dataset of 260 coronal sections were ~6.5 h and 8.5 h at *x-y* sampling of 2  $\mu\text{m}$  and 1  $\mu\text{m}$ , respectively (Supplementary Table 1). The 20 $\times$  objective (1.0 NA) enabled visualization of dendritic spines and fine axonal ‘arborizations’ (Fig. 1 and Supplementary Figs. 2–3; note that in this application we detected axons in single *x-y* optical sections, but not traced in the *z* dimension because of the spacing of 50  $\mu\text{m}$  between each section). The data collection times for a 260-section dataset using the 20 $\times$  objective were ~15.5 h and 24 h at *x-y* sampling of 1  $\mu\text{m}$  and 0.5  $\mu\text{m}$ , respectively (Supplementary Table 1). These experiments showed that STP tomography can be used as an automated method to collect high-resolution datasets of fluorescently labeled mouse brains.

Transgenic mice with cell type-specific fluorescent protein expression allow easy identification of different types of neurons and glia<sup>5</sup>. Next, we performed whole-brain mapping of different cell types in two bacterial artificial chromosome transgenic mice and one gene-targeted (knock-in) mouse. The *Mobp-GFP*<sup>5</sup> mouse

<sup>1</sup>TissueVision, Inc., Cambridge, Massachusetts, USA. <sup>2</sup>Cold Spring Harbor Laboratory, Cold Spring Harbor, New York, USA. <sup>3</sup>Department of Brain and Cognitive Sciences, Massachusetts Institute of Technology, Howard Hughes Medical Institute, Cambridge, Massachusetts, USA. <sup>4</sup>These authors contributed equally to this work. Correspondence should be addressed to P.O. (osten@cshl.edu).

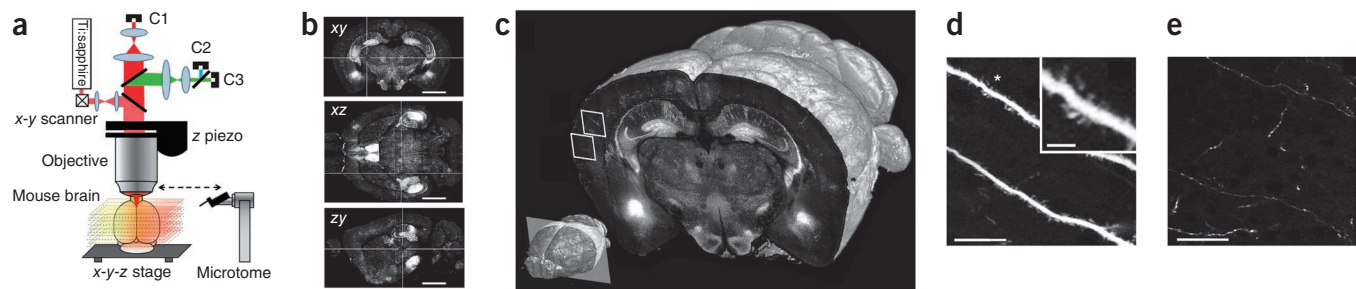


**Figure 1** | STP tomography. (a) Scheme of the method. A mouse brain is shown on *x-y-z* stage under a two-photon microscope equipped with Ti:sapphire laser, three photomultiplier tubes (C1–C3) for multicolor imaging and an objective scanner (*z* piezo) for *z*-stack imaging. The horizontal planes through the brain indicate the interleaved steps of imaging and sectioning. (b) Coronal (top), horizontal (middle) and sagittal (bottom) views of the *Thy1-GFP* dataset of 260 coronal sections after 3D reconstruction. White lines indicate *x-y-z* planes of view. Scale bars, 2 mm. (c) A 3D view of a coronal section of the GFPM brain imaged with a 20× objective at 0.5  $\mu\text{m}$  *x-y* sampling. Inset, position of the coronal plane in the imaged mouse brain (approximately –2.5 mm from the Bregma). (d,e) Enlarged views of the regions marked in c, demonstrating visualization of dendritic spines (d, top region marked in c) and fine axon fibers (e; bottom). Asterisk in d marks the region shown in the inset. Scale bars, 25  $\mu\text{m}$  (d,e) and 5  $\mu\text{m}$  (inset in d).

reveals a pattern of whole-brain myelination as a result of GFP expression in oligodendrocytes from the promoter of myelin-associated oligodendrocyte basic protein (Mbp) (Supplementary Video 3). The *Chat-GFP*<sup>5</sup> mouse allows visualization of whole-brain cholinergic innervation as a result of GFP expression in cholinergic neurons from the choline acetyltransferase (*Chat*) promoter (Supplementary Video 4). The *Sst-IRES-Cre::Ai9* mouse<sup>6</sup> reveals brain-wide distribution of somatostatin-expressing interneurons as a result of Cre recombinase expression from the somatostatin (*Sst*) gene<sup>6</sup> (*IRES* is the internal ribosome entry site sequence and *Ai9* is Supplementary Video 5). These experiments show the ease of generating brain atlas-like datasets of cell-type distribution and innervation by somatostatin tomography in transgenic mice. In addition, a more complete visualization of a specific cell-type distribution can be achieved by imaging *z*-stack volumes, instead of single optical sections, between the steps of mechanical tissue sectioning. As an example of this application, we imaged 800 optical sections (2.5  $\mu\text{m}$  *z* spacing), revealing the distribution of all somatostatin-expressing interneurons in the olfactory bulbs of the *Sst-IRES-Cre::Ai9* mouse<sup>6</sup> (Supplementary Videos 6 and 7). Imaging with high *z* resolution, of course, increases the acquisition time, and currently it would take about 7 d to image a whole mouse brain at the same resolution. However, increasing the imaging speed (at present 0.4  $\mu\text{s}$  pixel residence

time) by, for example, integration of resonant scanners, should make high *z*-resolution imaging of whole mouse brains by STP tomography more practical in the future.

In final experiments, we used STP tomography to map brain connectivity by imaging mouse brains injected with anatomical tracers in the somatosensory barrel cortex, a brain region with projections well documented by both retro- and anterograde tracing<sup>7,8</sup>. We imaged brains injected with cholera toxin B subunit (CTB)–Alexa Fluor 488 for retrograde tracing and adeno-associated virus expressing GFP (AAV-GFP) for anterograde tracing at 1  $\mu\text{m}$  *x-y* resolution (20× objective). As expected, we found Alexa Fluor 488–labeled neurons in brain areas known to project to the mouse barrel cortex<sup>7,8</sup> and detected GFP-labeled axons in brain areas known to receive barrel cortex projections<sup>7</sup> (Figs. 2 and 3 and Supplementary Figs. 4 and 5). The experiments also revealed two brain regions with sparse labeling that had not been reported in literature previously: retrogradely labeled contralateral orbital cortex and anterogradely labeled contralateral motor cortex (Supplementary Figs. 4b and 5b). Taken together, the replication of the previously described pattern of connectivity and the detection of putative new connections in

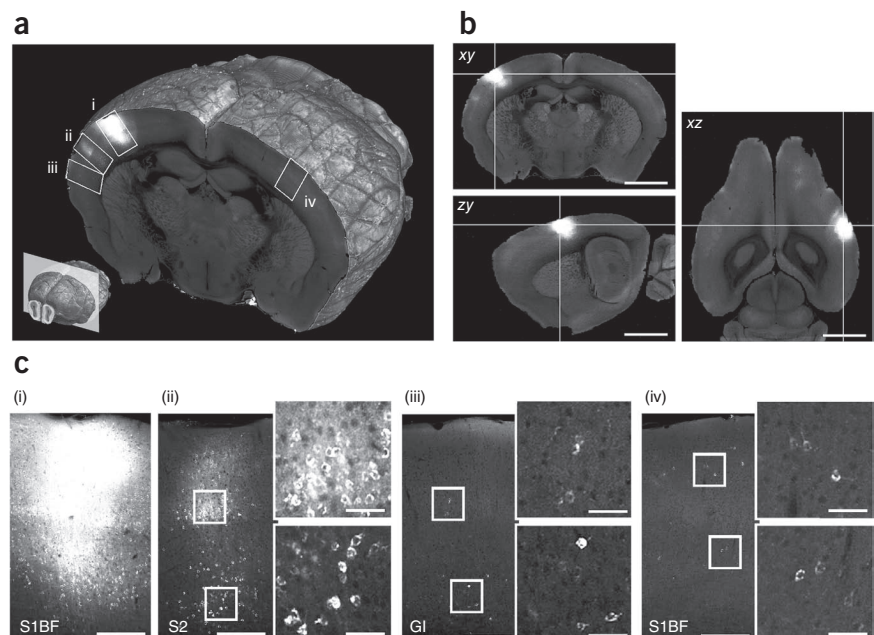
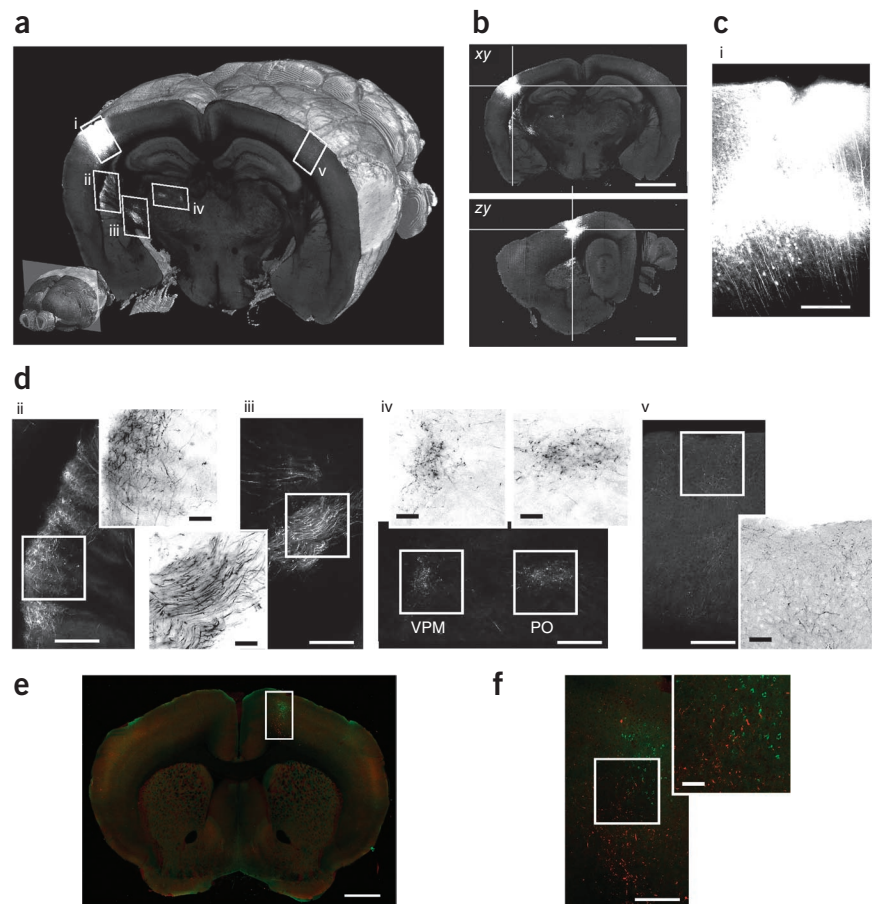


**Figure 2** | Retrograde tracing by CTB–Alexa Fluor 488. (a) A 3D view of a coronal section comprising the injection site (i) and several retrogradely labeled regions (ii–iv). Inset, position of the section in the whole brain (approximately –1.15 mm from Bregma). (b) Coronal (top), sagittal (bottom) and horizontal views of the injection site. Scale bars, 2 mm. (c) Cortical regions marked in a: the injection site in the barrel field of the primary somatosensory cortex (S1BF; i), ipsilateral secondary somatosensory cortex (S2; ii), granular insular cortex (GI; iii) and contralateral S1BF (iv). Also enlarged regions from supragranular and infragranular cortical layers (insets) of CTB-labeled cells are shown. Scale bars, 250  $\mu\text{m}$  (50  $\mu\text{m}$  in the enlarged view of ii, iii and iv).

**Figure 3** | Anterograde tracing by AAV-GFP and brain warping. **(a)** A 3D view of a coronal section comprising the injection site (i) and several anterogradely labeled regions (ii–v). Inset, position of the section in the whole brain (approximately  $-1.9$  mm from Bregma). **(b)** Coronal (top) and sagittal (bottom) views of the injection site. Scale bars, 2 mm. **(c)** Image of the injection site (marked i in **a**; S1BF). Scale bar, 250  $\mu$ m. **(d)** Images of brain regions (marked ii–v in **a**): ipsilateral caudoputamen (ii); axon fibers in the internal capsule (iii); ventral posteromedial thalamus (VPM) and posterior thalamus (PO) (iv); and (v) contralateral barrel cortex (S1BF). The enlarged views show inverted grayscale images for better visualization of axon fibers and varicosities. Scale bars, 250  $\mu$ m. **(e)** One section from a combined ‘virtual’ two-tracer dataset generated by warping data for the AAV-GFP-injected brain onto that of the CTB–Alexa Fluor 488-labeled brain. Scale bar, 1 mm. **(f)** Image of the brain region boxed in **e** comprising motor cortex (M1) with overlapping anterograde (AAV-GFP, red) and retrograde (CTB–Alexa Fluor 488, green) labeling. Scale bars, 250  $\mu$ m.



the contralateral cortical areas demonstrate that STP tomography is both a high-throughput and highly sensitive method for studies of whole mouse brain anatomy. The three-dimensional (3D) alignment of the datasets, in addition, facilitates direct comparison between different samples. We demonstrated this by warping data for the AAV-GFP-injected brain onto that for the brain labeled with CTB–Alexa Fluor 488 for direct comparison of anterograde and retrograde tracings (**Fig. 3**, Online Methods and **Supplementary Video 8**). We estimated the precision of registration of anatomical landmarks between two brains to be  $\sim 100$   $\mu$ m (**Supplementary Fig. 6**). Warping of multiple brains to one space is thus a simple alternative to using multiple tracer injections and can be extended to include many brains in a virtual brainbow<sup>9</sup>-like tracing.

STP tomography is part of a growing field of automated methods for *ex vivo* imaging of animal (mainly mouse) brain tissue<sup>1,3,10–14</sup>. The combination of serial imaging and sectioning has been pioneered by block-face imaging in light microscopy<sup>15</sup> and more recently adapted for two-photon microscopy<sup>3,4</sup>, confocal microscopy<sup>16</sup> and electron microscopy<sup>10</sup>. The use of two-photon microscopy allows deep tissue imaging, which is advantageous for focusing below the surface to obtain undisturbed optical sections and to collect high-resolution *z* stacks between sectioning steps, as pioneered in all-optical histology<sup>3</sup>.

What are the advantages of STP tomography compared to other methods for whole-mouse-brain imaging? First, robotized wide-field fluorescence microscopy of mounted serial brain sections<sup>1</sup> is more laborious and prone to error because it requires brain sectioning and mounting of the sections on microscope slides. In addition, enhancements in scanning speed of STP tomography should allow the use of our method for complete whole-brain anatomical tracings and cell counts, whereas imaging of cut tissue sections will always result in some loss of data.

Second, light-sheet fluorescence microscopy (also known as selective-plane illumination microscopy<sup>17</sup> and ultramicroscopy<sup>11</sup>), which can be used to image mouse brains without mechanical sectioning, but at a lower resolution<sup>11</sup> compared to our method. Until now, the use of light-sheet fluorescence microscopy for whole-mouse-brain imaging has also been limited by the need for chemical clearing that quenches fluorescent proteins, but this may be overcome by the development of improved clearing reagents<sup>18</sup>. Third, micro-optical sectioning tomography<sup>14</sup> (also known as knife-edge scanning microscopy<sup>13</sup>), which combines bright-field line-scan imaging and ultra-microtome cutting and was used to image mouse brains with stained Golgi in two studies<sup>13,14</sup>, has yet to be implemented for fluorescence microscopy. As tissue preparation requires dehydration and plastic embedding, which decrease GFP intensity, it is not clear how micro-optical sectioning tomography will perform for anatomical tracing and other applications described in our study.

In summary, STP tomography can be used to generate high-resolution anatomical datasets that can be readily warped for comparison of multiple brains. STP tomography is particularly well-suited for systematic studies of brain anatomy in genetic mouse models of cognitive disorders, such as autism and schizophrenia. To provide quantitative measurements for such studies, we are now focusing on anatomical registration<sup>19</sup> and the development of computational methods for detection of fluorescence signals in whole-brain datasets generated by STP tomography.



## METHODS

Methods and any associated references are available in the online version of the paper at <http://www.nature.com/naturemethods/>.

Note: Supplementary information is available on the Nature Methods website.

## ACKNOWLEDGMENTS

We thank Y. Bao and R. Palaniswamy for expert technical assistance, S.C. Chen and M. Culpepper for design of the flexure-based microtome, Z.J. Huang (Cold Spring Harbor Laboratory) for the *Sst-IRES-Cre::Ai9* mouse, W. Denk, K. Rockland and F. Scalia for critical reading of the manuscript, and J. Kuhl for preparing art graphics and animation. This work was supported by Simons Foundation grant (137480) to P.O., McKnight Technological Innovations in Neuroscience Award to P.O., Howard Hughes Medical Institute Collaborative Innovation award 43667 to H.S.S., and US National Institutes of Health grants 1 R43 HL093897-01 to T.R., R43 CA097670-01 and R44 CA097670-02 to T.R., K.B. and J.S.

## AUTHOR CONTRIBUTIONS

J.S., T.R., K.B. and P.O. planned the redesign of the instrument; T.R., J.S. and K.B. engineered and built the instrument; T.R. and J.S. wrote the operating software; L.R.K. did all imaging experiments; J.T. contributed to early imaging experiments; Y.K. validated warping accuracy; K.U.V. and I.A.-C. set up all image-processing methods; H.S.S. supervised image processing; T.R. and K.B. contributed to writing instrument portions of the paper; and P.O. supervised imaging, coordinated all work and wrote the paper.

## COMPETING FINANCIAL INTERESTS

The authors declare competing financial interests: details accompany the full-text HTML version of the paper at <http://www.nature.com/naturemethods/>.

Published online at <http://www.nature.com/naturemethods/>.

Reprints and permissions information is available online at <http://www.nature.com/reprints/index.html>.

1. Lein, E.S. *et al. Nature* **445**, 168–176 (2007).
2. Bohland, J.W. *et al. PLoS Comput. Biol.* **5**, e1000334 (2009).
3. Tsai, P.S. *et al. Neuron* **39**, 27–41 (2003).
4. Ragan, T. *et al. J. Biomed. Opt.* **12**, 014015 (2007).
5. Gong, S. *et al. Nature* **425**, 917–925 (2003).
6. Taniguchi, H. *et al. Neuron* **71**, 995–1013 (2011).
7. Aronoff, R. *et al. Eur. J. Neurosci.* **31**, 2221–2233 (2010).
8. Hoffer, Z.S., Arantes, H.B., Roth, R.L. & Alloway, K.D. *J. Comp. Neurol.* **488**, 82–100 (2005).
9. Livet, J. *et al. Nature* **450**, 56–62 (2007).
10. Denk, W. & Horstmann, H. *PLoS Biol.* **2**, e329 (2004).
11. Dodt, H.U. *et al. Nat. Methods* **4**, 331–336 (2007).
12. Micheva, K.D. & Smith, S.J. *Neuron* **55**, 25–36 (2007).
13. Mayerich, D., Abbott, L. & McCormick, B. *J. Microsc.* **231**, 134–143 (2008).
14. Li, A. *et al. Science* **330**, 1404–1408 (2010).
15. Odgaard, A., Andersen, K., Melsen, F. & Gundersen, H.J. *J. Microsc.* **159**, 335–342 (1990).
16. Sands, G.B. *et al. Microsc. Res. Tech.* **67**, 227–239 (2005).
17. Huisken, J., Swoger, J., Del Bene, F., Wittbrodt, J. & Stelzer, E.H. *Science* **305**, 1007–1009 (2004).
18. Hama, H. *et al. Nat. Neurosci.* **14**, 1481–1488 (2011).
19. Hawrylycz, M. *et al. PLoS Comput. Biol.* **7**, e1001065 (2011).

## ONLINE METHODS

**Tissue preparation.** The following mouse strains were used: Gene Expression Nervous System Atlas (GENSAT) *Chat-GFP* strain *Tg(Chat-EGFP)GH293Gsat/Mmcd*; (stock number 000296-UCD) and *Mobp-GFP* strain *Tg(Mobp-EGFP)IN1Gsat/Mmcd* (stock number 030483-UCD)<sup>5</sup> (Mutant Mouse Regional Resource Centers; MMRRC); *Thyl-GFP* (line M)<sup>20</sup>; *Sst-IRES-Cre::Ai9* (ref. 6); and wild-type C57BL/6J (Jax mice; 000664). As anatomical tracers, we used CTB–Alexa Fluor 488 (Invitrogen; 0.5% (w/v) in phosphate buffer) and AAV–GFP with synapsin promoter<sup>21,22</sup>. AAV was produced at the Salk vector core as a chimeric 1/2 serotype<sup>23</sup>, purified by iodoxinal gradient and concentrated to  $5.3 \times 10^{11}$  genomic copies per milliliter. Stereotaxic injections of the tracers were done as described previously<sup>24</sup>. Briefly, the mice were anesthetized by 1% isoflurane inhalation. A small craniotomy (~300 × 300 μm) was opened over the left primary somatosensory cortex and ~50 nl of virus or 50 nl of 0.05% CTB–Alexa Fluor 488 was injected into layer 2/3 barrel cortex at stereotaxic coordinates: caudal 1.6, lateral 3.2, ventral 0.3 mm relative to bregma. The skin incision was then closed with silk sutures, and the mice were allowed to recover with free access to food and water (meloxicam was given at 1 mg kg<sup>-1</sup> subcutaneously for analgesia). The brains were prepared for imaging 10–14 d later (see below). Animal procedures were approved by the Cold Spring Harbor Laboratory Animal Care and Use Committee and carried out in accordance with US National Institutes of Health standards.

The mouse brains were prepared for STP tomography as follows. The mice were deeply anesthetized by intraperitoneal (i.p.) injection of the mixture of ketamine (60 mg kg<sup>-1</sup>) and medetomidine (0.5 mg kg<sup>-1</sup>) and transcardially perfused with ~15 ml cold saline (0.9% NaCl) followed by ~30 ml cold neutral buffered formaldehyde (NBF, 4% (w/v) in phosphate buffer, pH 7.4). The brains were dissected out and kept in 4% NBF overnight at 4 °C. To decrease formaldehyde-induced autofluorescence, the brains were incubated in 0.1 M glycine (adjusted to pH 7.4 with 1 M Tris base) at 4 °C for 2–5 d. The brains were then washed in phosphate buffer and embedded in 3–5% oxidized agarose as described<sup>25,26</sup>. Briefly, agarose type I (Sigma) was oxidized by stirring in 10 mM sodium periodate (NaIO<sub>4</sub>, Sigma) solution for 2 h at room temperature (20–25 °C), washed 3x and resuspended in phosphate buffer to bring the final concentration to 3–5%. The mouse brain was pat-dried and embedded in melted oxidized agarose using a cube-shaped mold. Covalent cross-linking between brain surface and agarose was activated by equilibrating in excess of 0.5–1% sodium borohydride (NaBH<sub>4</sub>, Sigma) in 0.05 M sodium borate buffer (pH 9.0–9.5), gently shaking for 2–4 h at room temperature (or overnight at 4 °C) (note that after rinsing, activated agarose can be stored in phosphate buffer at 4 °C for up to 1 week; sodium borohydride buffer should be prepared fresh). Covalent cross-linking of the agar–brain interface is important to keep the brain firmly embedded during sectioning and to limit shadowing artifacts by insufficiently cut meninges (see below).

**Instrument and software.** The experiments were performed on a high-speed multiphoton microscope<sup>27</sup> with integrated vibratome sectioning (TissueCyte 1000, TissueVision; **Supplementary Video 1** shows the instrument schema). Laser light from a titanium-sapphire laser (Chameleon Ultra, Coherent) is directed through a tube and scan lens assembly toward a pair

of galvanometer mirrors (6210H, Cambridge Technology) and reflected by a short pass dichroic toward a microscope objective (either a 20× Olympus XLUMPLFLN20XW lens, NA 1.0, or a 10× Olympus XLUMPLFL10XW-SP lens, NA 0.6). The fluorescent signal from the sample is collected by the same objective, passes through the dichroic and is directed by a series of mirrors and lens onto a photomultiplier tube (PMT) detection system (Hamamatsu, R3896). In two- and three-channel multicolor configuration the emission light is split by dichroic mirror(s) onto, respectively, two and three PMTs to allow for simultaneous multi-channel data acquisition. The 3D scanning of z-volume stacks was achieved via a microscope objective piezo (PI E-665 LVPZT amplifier, P-725 PIFOC long-travel objective scanner), which translates the microscope objective with respect to the sample. Laser light intensity can be varied by liquid crystal controller (Thorlabs, LCC25) for shuttering purposes and as a function of imaging depth into the sample.

Robust mechanical sectioning was achieved by a vibrating blade microtome integrated into the imaging system. It was based on a new dual-flexure design. Flexures are compliant mechanisms consisting of a series of rigid bodies connected by compliant elements that are designed to produce geometrically well defined motion upon application of force. Flexures can achieve smooth displacements down to the sub-micrometer level with little parasitic motion. The microtome consists of a primary flexure to which the blade is mounted and a secondary flexure, which connects the primary flexure to the actuator. The actuator consists of a direct current (DC) motor with an off-center cam attached to the shaft. The secondary flexure is designed to be rigid in the direction of the cut and compliant in all other directions. In this way, only a force along the direction of the cut is transmitted to the primary flexure which holds the microtome blade and reduces any potential parasitic motion along unwanted axis of motion. For this design, we experimentally verified that the parasitic z vertical deflection was less than 2 μm root mean square (r.m.s.) by measuring the motion directly with capacitive sensors. Additional details of the microtome design will be presented in the future (S.-C. Chen and M. Culpepper, unpublished data). The vibration frequency can be set to 0–60 Hz and the blade angle to 5–30 degrees. By the use of different cams, the amplitude can be adjusted from 0.8 mm to 2 mm. We empirically determined the sectioning parameters for brain tissue to be 0.8 mm amplitude at 60 Hz and at a blade angle of 11 degrees (the blade was Vibroslice from WPI). The reliability of sectioning was verified by measurements of the brain surface and overlapping z-planes before and after sectioning during a whole brain dataset (**Supplementary Fig. 7**). To achieve reliable sectioning it is essential to use brains covalently cross-linked in oxidized agarose (see above).

The instrument was controlled by custom software, written in C++ and C#. The software handles the scanning, stage motion, microtome control and data acquisition. The software is composed of several discrete services, each of which controls a particular hardware component or function of the instrument. Sequences of events are coordinated by a master orchestrator service. For instance, to scan a section, a command is sent from the orchestrator service to the galvanometer scanner service commanding it to unshutter the laser and scan an image. The orchestrator service waits until the scanner service reports that the image acquisition has been completed and then sends

a command to the  $x$ - $y$  stages to move the sample to the next position. Once the  $x$ - $y$  stages complete the requested motion, a command is sent back to the orchestrator service, which in turn issues a command to the scanner service to acquire a second image. During the imaging, background services handle the data acquisition and saving of the 16-bit TIFF images to a local or network attached storage device. The process continues until an entire section has been acquired. Similarly, to acquire a whole-brain dataset, at the end of each mosaic section acquisition the orchestrator service commands the  $z$ -stage service to move the sample upwards by the desired slice thickness. Simultaneously, the sample is directed toward the microtome by the  $x$ - $y$  stage service. Once in position, the microtome is turned on and the sample is translated through the microtome and a tissue section is cut. The sample is then translated back underneath the objective, and the next section is imaged. This process repeats until all sections are imaged. The software is highly modular and additional services can be introduced or specific hardware can be exchanged with minimal changes to higher level routines. For instance, services to automate additional features, such as the capture of the slices after sectioning, can be added in the future.

In comparison to an earlier prototype<sup>4</sup> there are several improvements in the design of the current instrument. The previous version used a milling machine to machine the surface of a paraffin embedded tissue. Because paraffin quenches fluorescence, an integrated vibrating blade microtome (**Supplementary Video 1**) is now used. This allows imaging of formaldehyde fixed brains embedded in agar, a histological procedure with low quenching. As an additional advantage, the sections can be used for further histochemical analysis as they are no longer destroyed by the milling process (currently, the sections sink to the bottom of the water bath and can be collected and sorted at the end of the experiment). The incorporation of low-magnification (10–20 $\times$ ) high-numerical aperture (NA 0.6–1.0) lenses has increased fluorescence collection compared to a standard 60 $\times$  objective, without compromising the resolution at large imaging depths<sup>28</sup>. The combination of a low-magnification lens with large-aperture optics have increased the image field of view that can be scanned with even illumination from  $\sim 200$   $\mu\text{m}$  to 1,400  $\mu\text{m}$ . High-speed galvanometric scanning has replaced a polygonal scanning approach. Galvanometric scanners are far more flexible than polygonal scanners and allow a wide range of pixel sizes and residence times to be set depending on the requirements of the sample. Finally, high speed  $x$ - $y$ - $z$  stages were constructed to allow positioning of the sample over centimeters of travel with sub-micrometer accuracy. The custom  $z$ -stage was designed to hold two commercial  $x$  and  $y$  stages (Polytech, PI) and be rotationally rigid with a pitch and yaw of less than 1  $\mu\text{m}$  over the entire travel range of the  $x$  and  $y$  stage assembly. The  $x$  and  $y$  axes have a 0.1  $\mu\text{m}$  positional accuracy, a settling time of 0.1 ms and a speed up to 50  $\text{mm s}^{-1}$ . The high speed and small settling time allow for rapid positioning of the sample and minimizes acquisition time of a section, and the positional accuracy decreases post-processing registration time. The  $z$  axis has a precision of 0.15  $\mu\text{m}$ , maximum velocity of 1  $\text{mm s}^{-1}$  and maximum  $z$ -dimension travel distance 5 cm. As this stage is only used to raise the sample to the microtome blade and objective, its speed has negligible impact on the imaging time.

**Instrument operation.** Once the brain is positioned under the objective and the imaging and sectioning parameters are chosen (see below), the instrument operates in a fully automated mode. The brain is mounted in saline (we used 50 mM phosphate buffer, pH 7.4) in a water bath positioned on the computer controlled  $x$ - $y$ - $z$  stages. After identifying  $z$  position of the brain surface under the objective, the following parameters are set in the software: FOV size, FOV mosaic size, pixel size, pixel residence time, laser power, sectioning speed, sectioning frequency,  $z$  step for each sectioning cycle and a number of  $z$  sections. The imaging plane is set below the brain surface to ensure an undisturbed optical section throughout. We typically imaged 50  $\mu\text{m}$  below surface, but a comparable image resolution can be obtained down to  $\sim 100$   $\mu\text{m}$  below surface with small adjustments in laser power. The laser power is set constant for imaging of single optical sections between each sectioning steps. For collection of  $z$ -volumes between sectioning steps, such as the dataset of *Sst-IRES-Cre::Ai9* olfactory bulb imaged at  $z$ -resolution 2.5  $\mu\text{m}$  (**Supplementary Video 6**), the laser power is adjusted based on the  $z$  depth to compensate for increased light scattering with increased depth.

The number of FOV tiles per mosaic is set to cover the extent of the sample and allow for a small overlap between the FOV tiles for post-processing stitching (see below). In experiments with the 10 $\times$  objective, we used  $6 \times 8$  overlapping mosaic of 1.66  $\text{mm} \times 1.66$   $\text{mm}$  FOV, the  $x$ - $y$  stage movement is 1.5  $\text{mm}$ , pixel size 1  $\mu\text{m}$  or 2  $\mu\text{m}$  and pixel residence time of 0.4–1.0  $\mu\text{s}$ . In experiments with the 20 $\times$  objective we used  $11 \times 17$  mosaic of 0.83  $\text{mm} \times 0.83$   $\text{mm}$  FOV, the  $x$ - $y$  stage movement is 0.7  $\text{mm}$ , pixel size 0.5  $\mu\text{m}$  or 1  $\mu\text{m}$  and pixel residence time between 0.4  $\mu\text{s}$  and 1  $\mu\text{s}$ . Once a mosaic is completed, the same  $x$ - $y$ - $z$  stages used for the mosaic imaging move the sample from the microscope objective toward a vibrating blade microtome to section the uppermost portion of the tissue. The times for imaging of 260-section mouse brain datasets are listed in **Supplementary Table 1**.

**Image processing.** The images were constructed from the PMT signal, with the tile and pixel size set by a combination of the scan angle and pixel sampling rate. The tiles were saved as tif files (named as Tile\_Z{zzz}\_Y{yyy}\_X{xxx}.tif) and processed as follows. First, each tile is cropped to remove illumination artifacts near the edges (the number of pixels cropped is determined empirically based on the objective used and FOV; for example, we cropped 15 pixels and 10 pixels at each side of  $x$  and  $y$  direction, respectively, for  $832 \times 832$  pixel FOV). Second, all tiles from one brain dataset (for example 52,360 tiles for  $11 \times 17$  mosaic of 280 sections) are loaded in Fiji (ImageJ-based image-processing software; <http://fiji.sc/wiki/index.php/Fiji>) and used to generate an average-intensity image for illumination correction by a  $z$ -project function. Third, all tiles are divided by the average-intensity image to correct for uneven illumination (Plugins > TissueVision > Divide sequence by image). Fourth, illumination-corrected tiles are used to stitch the sequence of mosaic images (Plugins > Stitching > Stitch Sequence of Grids of Images; fusion method = linear blending, fusion alpha = 1.5, regression threshold = 0.3, max/avg displacement = 2.5, absolute displacement = 3.5; select “compute overlap”). The transformation between the tiles is modeled as a translation transform. For each section, the  $x$  and  $y$  translations are determined by cross correlation<sup>29</sup> between the tiles. At the overlapping regions, the pixels are blended linearly<sup>30,31</sup>.

The overlapping regions may show some photobleaching when large power (>150 mW) is used for samples with low fluorescence. In such case, as bleaching occurs mainly for the second overlapping tile, it is better to display the image from the first tile and use the second tile only for *x-y* registration. This can be achieved by rendering the tiles into the mosaic in the reverse order they were scanned by the microscope: the pixels of the first scanned tile overwrite the same pixels scanned later in the second. The whole brain dataset of  $11 \times 17$  mosaic of 280 sections of raw tiles scanned at a 16-bit depth occupies ~40 gigabytes (Gb). The final stitched slices occupy ~25 Gb with LZW compression on the final stitched TIFF slices. All image processing was run on Mac/Linux desktop machines with at least 8 Gb on RAM.

**Image warping.** The warping was done by an affine registration followed by an elastic B-splinebased transformation<sup>32</sup> using autofluorescence signal from STP tomography datasets down-sampled by a factor of 20 (resolution  $20 \mu\text{m} \times 20 \mu\text{m} \times 50 \mu\text{m}$ ). The registration was done in a multiresolution approach for a more efficient and robust alignment<sup>33</sup>. The affine transform was calculated using 4 resolution levels while the elastic step uses 6 resolution steps. Advanced Mattes mutual information<sup>34</sup> was used as the metric to measure the similarity of registration. In this parametric registration method, Mattes Mutual information is used as the similarity measure between the moving and fixed images. The registration problem is posed as an optimization problem, where the image discrepancy/similarity function is minimized for a set of transformation parameters. The transformation parameters are then estimated in multi-resolution approach, which ensures a more robust approach compared to a single resolution approach. The image similarity function is estimated and minimized for a set of randomly chosen samples with the images at each resolution in an iterative way. On a 8 core central processing unit (CPU) with 16 Gb RAM, the registration takes 12 h on  $650 \times 450 \times 300$  voxel sized image with  $20 \mu\text{m} \times 20 \mu\text{m} \times 50 \mu\text{m}$  pixel spacing. The entire image warping experiment is set up using elastix<sup>32</sup>, an image registration tool based on Kitware's ITK with Parameters set up according to our dataset. To determine the effectiveness of the warping procedure, we compared the displacement of 42 anatomical manually identified landmark points of interest in two mouse brain scans before and after warping one dataset onto the other (**Supplementary Fig. 6**). The mean ( $\pm$ s.e.m.) distance between the corresponding points in the two brains was  $749.5 \mu\text{m} \pm 52.1 \mu\text{m}$  and  $102.5 \mu\text{m} \pm 45 \mu\text{m}$  before and after warping, respectively.

**Troubleshooting.** We established STP tomography for imaging formaldehyde-fixed brains embedded in agar because this provides maximal preservation of GFP fluorescence. However, vibrating microtome-based sectioning of a relatively soft agar-brain block is mechanically more challenging than sectioning of hard resin-embedded tissue and can lead to imaging artifacts. First, the brain may become 'loose' in the agar block after many hours of imaging and this can cause the remaining part of the

brain to fall out of the agar or the brain edges to shift out of the imaging plane. These problems can be completely prevented by covalent cross-linking of brain-agar after embedding (see above). Second, brain meninges sometime fail to be completely cut with every sectioning step and the remaining small stripes of meninges can cause shadowing artifacts during imaging. This problem is again largely solved by brain-agar cross-linking, but small uncut meninges sometimes remain in the regions between hemispheres that are not in contact with agar (this is seen in a few sections in our datasets; an example from the Thy1-GFPM dataset is shown in **Supplementary Fig. 8a**). These artifacts are infrequent and only near the brain surface and thus are unlikely to have a substantial effect on data interpretation in most experimental applications. Carefully removing the meninges under a dissecting microscope will help to limit this problem. Third, in the current configuration of the instrument, cut brain sections freely sink to the bottom of the water bath. However, a floating section may sometimes remain between the objective and the brain block, causing substantial shadowing artifacts (an example from the Thy1-GFPM dataset is shown in **Supplementary Fig. 8b**). This happens infrequently (typically once per several samples) and can be largely avoided by setting a longer waiting time after each sectioning step in the instrument software (we used only a 1 s waiting time for fast data collection). Recent software update also added a lateral movement of the stage at the end of sectioning, which helps to direct the sinking section away from the objective. In addition, we are working on integrating a section retrieval module, which will allow an automated capture of each brain section and eliminate the problem with floating sections. Finally, meninges between the frontal cortex and the accessory olfactory bulb sometimes show very bright autofluorescence (an example from the Chat-GFP is shown in **Supplementary Fig. 8c**). This only occurs in the rostral brain areas, and because it is on the brain surface it does not affect data interpretation.

20. Feng, G. *et al.* *Neuron* **28**, 41–51 (2000).
21. Kugler, S., Lingor, P., Scholl, U., Zolotukhin, S. & Bahr, M. *Virology* **311**, 89–95 (2003).
22. Dittgen, T. *et al.* *Proc. Natl. Acad. Sci. USA* **101**, 18206–18211 (2004).
23. Hauck, B., Chen, L. & Xiao, W. *Mol. Ther.* **7**, 419–425 (2003).
24. Cetin, A., Komai, S., Eliava, M., Seeburg, P.H. & Osten, P. *Nat. Protoc.* **1**, 3166–3173 (2007).
25. Shainoff, J.R. *Glyoxal agarose and zonal immobilization of proteins therewith* (The Cleveland Clinic Foundation, 1982).
26. Sallee, C.J. & Russell, D.F. *Biotech. Histochem.* **68**, 360–368 (1993).
27. Denk, W., Strickler, J.H. & Webb, W.W. *Science* **248**, 73–76 (1990).
28. Oheim, M., Beaurepaire, E., Chaigneau, E., Mertz, J. & Charpak, S. *J. Neurosci. Methods* **111**, 29–37 (2001).
29. Kuo, D. & Girod, B. Direct estimation of displacement histograms. in *Proceedings of the Optical Society of America Meeting on Understanding and Machine Vision* 7376 (1989).
30. Preibisch, S., Saalfeld, S. & Tomancak, P. *Bioinformatics* **25**, 1463–1465 (2009).
31. Cardona, A. *et al.* *J. Neurosci.* **30**, 7538–7553 (2010).
32. Klein, S., Staring, M., Murphy, K., Viergever, M.A. & Pluim, J.P.W. *IEEE Trans. Med. Imaging* **29**, 196–205 (2010).
33. Lester, H. & Arridge, S.R. *Pattern Recognit.* **32**, 129–149 (1999).
34. Mattes, D., Haynor, D.R., Vesselle, H., Lewellen, T.K. & Eubank, W. *IEEE Trans. Med. Imaging* **22**, 120–128 (2003).